Ultrasonics Sonochemistry 76 (2021) 105651

Contents lists available at ScienceDirect

Ultrasonics Sonochemistry

journal homepage: www.elsevier.com/locate/ultson

# Micron-sized particle separation with standing surface acoustic wave—Experimental and numerical approaches

Erfan Taatizadeh [a,b,c], Arash Dalili [a], Pamela Inés Rellstab-Sánchez [a], Hamed Tahmooressi [a], Adithya Ravishankara [a], Nishat Tasnim [a], Homayoun Najjaran [a], Isaac T.S. Li [b], Mina Hoorfar [a,*]

[a] School of Engineering, Faculty of Applied Science, The University of British Columbia, Kelowna, BC V1V 1V7, Canada
[b] Department of Chemistry, Irving K. Barber Faculty of Science, The University of British Columbia, Kelowna, BC V1V 1V7, Canada
[c] School of Biomedical Engineering, Faculties of Applied Science and Medicine, The University of British Columbia, Vancouver, BC V6T 1Z3, Canada

ARTICLE INFO

*Keywords:*
Surface acoustic wave
Acoustofluidics
Microfluidics
Finite element modeling
Particle separation

ABSTRACT

Traditional cell/particle isolation methods are time-consuming and expensive and can lead to morphology disruptions due to high induced shear stress. To address these problems, novel lab-on-a-chip-based purification methods have been employed. Among various methods introduced for the separation and purification of cells and synthetics particles, acoustofluidics has been one of the most effective methods. Unlike traditional separation techniques carried out in clinical laboratories based on chemical properties, the acoustofluidic process relies on the physical properties of the sample. Using acoustofluidics, manipulating cells and particles can be achieved in a label-free, contact-free, and highly biocompatible manner. To optimize the functionality of the platform, the numerical study should be taken into account before conducting experimental tests to save time and reduce fabrication expenses. Most current numerical studies have only considered one-dimensional harmonic standing waves to simulate the acoustic pressure distribution. However, one-dimensional simulations cannot calculate the actual acoustic pressure distribution inside the microchannel due to its limitation in considering longitudinal waves. To address this limitation, a two-dimensional numerical simulation was conducted in this study. Our numerical simulation investigates the effects of the platform geometrical and operational conditions on the separation efficiency. Next, the optimal values are tested in an experimental setting to validate these optimal parameters and conditions. This work provides a guideline for future acoustofluidic chip designs with a high degree of reproducibility and efficiency.

## 1. Introduction

The microfluidics-based cell/particle manipulation technologies have shown great potential due to low sample and reagent volume consumption, high product purity, high sensitivity, ease of use, and short isolation time [1–3]. Generally, microfluidic-based isolation methods are classified into two main groups: active and passive methods. In the first group, the isolation is performed by the action of external forces, while in the second one, the hydrodynamic and surface forces play the main roles in isolation [4,5]. The passive methods (such as filtration [6–8], immuno-affinity [9–12], inertial centrifugation [13], lateral displacement with nanopillar [14], and viscoelastic flow [15]) have higher throughput and also easier configuration as compared to the active methods. However, lower purity in biomolecules separation has been observed using passive methods compared to active methods. On the other hand, active methods use external forces that can be generated by the electrical field [6], magnetic field [9,12], and acoustic field [16,17] for biomolecules sorting and manipulation. The throughput of active methods is relatively lower than that of passive methods. The main disadvantage of active systems is that they require power and control.

The majority of the aforementioned active isolation methods rely on the size of the particles. Their main difference is the dependency of the acting forces on different physical properties of working samples. For example, the electrical permittivity and magnetic susceptibility determine the forces exerting on the particles in electrical and magnetic-based isolation methods [5]. However, similarities (in terms of the order and sign values) in the electrical permittivity of the particles and surrounding medium decrease the efficiency of the electrical-based isolation method significantly [18]. With a similar approach, the

* Corresponding author.
*E-mail address:* mina.hoorfar@ubc.ca (M. Hoorfar).

https://doi.org/10.1016/j.ultsonch.2021.105651
Received 17 February 2021; Received in revised form 11 May 2021; Accepted 18 June 2021
Available online 22 June 2021

magnetic-based isolation method can only be employed when the particles are magnetic. The acoustophoresis is the only active isolation method that addresses and overcomes these obstacles as it functions based on mechanical properties compared to electrical or magnetic properties.

The particle movement resulting from acoustics is denoted as acoustophoresis [19]. The acoustophoresis can be transferred easily in microfluidic devices as they provide the necessary working microscale medium. Acoustofluidic platforms (a combination of microfluidics and acoustics) are classified into three types based on the acoustic wave guiding process [20]: bulk acoustic wave (BAW) [21], surface acoustic wave (SAW) [22,23], and acoustic plate mode (APM) [22,24]. SAW has been widely used for various biological applications as BAW is mainly limited to high frequency, and APM is challenging to operate in a standard oscillator circuit [22]. SAWs are mechanical waves that primarily propagate upon the surface of an elastic material. These waves consist of a longitudinal compression motion coupled with a transversal shear motion [25–28]. The wave generation is achieved by interdigital transducers (IDTs), the comb-shape electrodes (characterized based on the number of electrode fingers and their length referred to as the aperture) patterned upon a surface of a piezoelectric material. SAW loses the energy due to the viscous damping induced by acoustic streaming flow (ASF) in the fluid and imparts an acoustic radiation force (*ARF*) to suspended particles [27,28]. There are two types of SAW: the traveling SAW (TSAW), generated when a SAW is radiated away from the IDT; and the standing SAW (SSAW), formed when two individual IDTs generate oppositely propagating identical TSAWs which interfere constructively [2,29,30]. Both types create *ARF* and *ASF* in the fluid. However, the main interest is to minimize the *ASF* effect to implement *ARF* dominated particle manipulation [31]. This goal can be achieved easier by SSAW as the *ASF* developed by oppositely propagating TSAWs cancel one another, and the overall strength of the *ASF* diminishes [28]. Besides, SSAW has better controllability and work with lower frequencies (there is defined special situation, e.g., a given liquid size) in comparison with TSAW (by an order of ~10 MHz in SSAW compare to ~100 MHz in TSAW) [32].

Although experimental studies have been extensively performed to demonstrate this technique for various microfluidic applications, numerical simulation of acoustophoresis driven by SAW has not been studied extensively. The numerical modeling is generally favorable as a pre-step for designing an acoustofluidic chip as it saves both time and cost. Most of the current numerical studies only considered a one-dimensional (1D) harmonic standing wave (HSW) modeling method to simulate the acoustic pressure distribution in the fluid [16,30,33]. Mao et al. [34] claimed that 1D HSW modeling causes some discrepancies in the estimated acoustic pressure distribution inside the microchannel compared to the experiments. The difference between the actual distribution and that modeled using 1D HSW is mainly caused by the longitudinal waves when SSAW is leaking into the fluid and the PDMS wall of the microchannel. Thus, it is highly desirable to establish an accurate representation of the acoustic pressure distribution originating from SSAW inside the microfluidic channel. Some attempts have been made to improve the accuracy of the numerical simulation by considering 2D HSW modeling [35]. More recently, Nama et al. [36] calculated the first-order fields that drive the acoustic streaming and the time-averaged acoustic radiation forces acting on suspended particles using a 2D numerical simulation. However, they simplified the system by employing the effect of the piezoelectric substrate instead of modeling it as a separate domain. This simplification adds an some bias to the estimated acoustic pressure as the internal energy dissipation in the piezoelectric is ignored. As a result, the energy dissipations caused by the PDMS domain were not precisely modeled as neither the PDMS domain was included in the simulation nor the impedance boundary condition was applied to the microchannel walls. In another study, Hsu et al. [37] investigated the application of dual-wavelength standing surface acoustic waves for controlling particle migration towards the microchannel. Similar to other studies [36,38,39], the work of this group was limited to the fluid domain, and the influence of the PDMS walls and the influence of the piezoelectric domain were not well understood.

Most of the previous research focused on experimental designing and testing were solely based on trial-and-error processes. For instance, the number of the electrode fingers and the aperture length in an IDT are suggested to be in the range of 50 to 100 and at least 30 times the wave wavelength, respectively [40]. Considering these rough estimates for parameters affecting the efficiency of SSAW devices significantly, there is a need for the development of an efficient numerical model capable of optimizing the preliminary designing factors of acoustofluidic chips. By employing the optimized parameters involved in developing the acoustofluidic chip, precise particle/cell manipulation and separation can be achieved.

In this paper, the capability of the acoustofluidic chip as a precise and fast-acting platform for the manipulation of particles was demonstrated. Various steps were taken into account to achieve this goal, including parameter optimization, 2D numerical simulation, and experimentation. As the first step, the proposed chip was studied parametrically by a finite element analysis (FEA) method. Next, the calculated optimal values of the parameters were implemented in our designs to validate the outcomes of the numerical simulation with the experimental tests. Both experimental and numerical simulation results demonstrated that the number of IDT fingers and the applied voltage play the most important roles in increasing separation efficiency. However, there is a threshold for the applied voltage due to the joule heating phenomenon. According to the results, the voltage of $15.0V$ is the maximum value that should be supplied to the chip to ensure stable tests. Additionally, it was shown numerically that only the number of IDT fingers of $\{20, 50, 80\}$ provides the highest energy transfer, and a small variation from the optimum value can cause a substantial reduction in *ARF*. Additionally, results revealed that the large microchannel's height (bigger than the acoustic wavelength) leads to the horizontal particle movements and the vertical migration inside the microchannel. These results show that 1D HSW simulations cannot predict the particle movement accurately, and there is always a bias in the results of such simulations. In fact, using the optimized parameters presented here for the development of the acoustofluidic chip, a precise and controllable manner in particle/cell manipulation and separation can be achieved.

## 2. Numerical simulation results

The commercialized finite element analysis (FEA) software package (COMSOL Multiphysics, version 5.4) was used to simulate the SAW propagation in the $LiNbO_3$ substrate and its penetration (Leaky SAW) in the PDMS and fluid. The SSAW field is derived by solving Eqs. (S6) - (S8) using a frequency-based solver. The distribution of the particles was then calculated by coupling the derived SSAW field in the fluid in a time-depended manner. The 2D computational domain is shown in Fig. S7.

### 2.1. Mesh independency analysis

To save computational resources and time, the mesh size is decreased at the piezoelectric substrate and progressively increased closer to the bottom of the substrate (as most of the relevant physics is close to the top surface). The maximum magnitude of the acoustic pressure (*AP*) was used as the parameter for the mesh-independency analysis. Results indicated that a coarse mesh size of $\frac{1}{5}\lambda_{SAW}$ near the bottom of the piezoelectric substrate and a fine mesh with the size of $\frac{1}{10}\lambda_{SAW}$ in the PDMS domain, the microchannel and near the top of the piezoelectric substrate can provide the required accuracy and fulfill the mesh-independency for the numerical results.

### 2.2. PDMS wall boundary condition

To find the appropriate wall boundary condition (BC), hard and lossy (impedance) boundary PDMS walls were considered as separate domains with the same device characteristic (to eliminate the bias for the numerical simulation). The value of parameters are as follows: $\lambda_{SAW} = 150\ \mu m$, $V_0 = 20V$, $N_P = 20$, Microchannel's height $= 100\ \mu m$, Microchannel's width $= 800\ \mu m$, PDMS's width $= 3\ mm$, and PDMS's height $= 1\ mm$. The results in Fig. 1 demonstrate that the hard-wall BC changes (See Video S1) the locations of PNs and PANs while the lossy-wall BC (See Video S2) increases the maximum value of the acoustic pressure (~68% higher). However, there is a third option: considering the PDMS walls as the separate domain and including its thickness of the walls (See Video S3) which results in the dissipation of the majority of the acoustic energy into PDMS before reaching the fluid. This option is more realistic, and the results obtained using this option are in better agreement with previous studies [34,36,41]. Considering this option results in the maximum value of *AP* lower than that obtained for the case of the lossy-wall BC and still higher than that obtained for the hard-wall BC. Nevertheless, using either assumption of the lossy wall or PDMS does not disrupt the morphology of PNs and PANs, indicating these methods to be good candidates for simulations. In this study, due to the advantages of the PDMS as a separate domain in comparison to other types of BCs, we have chosen it for further steps in our simulation.

### 2.3. Effects of width and height of the microchannel

In acoustofluidic, one of the most important parameters is the dimension of the microchannel. Previous studies [34,36,41] have shown that a small mismatch in the alignment of the microchannel in the bonding process can disrupt the positioning of the PNs and PANs in the designed acoustofluidic chip. Previous research has assumed that the factor determining the PNs and PANs locations is the microchannel width. For instance, to have one PN in the microchannel, the width of the microchannel must be equal to $\lambda_{SAW}/2$, while the width should be $\lambda_{SAW}$ for two PNs. Herein, we carried out the parametric study to calculate the distribution of *AP* at various heights and widths of the microchannel. It is worth mentioning that the microchannel was shifted by $\lambda_{SAW}/4$ from the center of the delay line to locate one PN in the middle of the microchannel.

In general, the maximum amplitude of *AP* occurs in PANs, where the mechanical displacement is maximized, while the location of PNs is determined where the minimum mechanical displacement occurs (See Videos S4 and S5). The value of parameters are as follows: $\lambda_{SAW} = 150\ \mu m$, $N_P = 20$, PDMS's width $= 3\ mm$, and PDMS's height $= 1\ mm$. Fig. 2 demonstrates the effects of the width and height of the microchannel on the locations of the PNs and PANs. Each graph in Fig. 2 represents the contour of positive values (red) and negative values (blue), called dipole *AP*, along with zero values (white) of *AP* at different heights and widths of the microchannel. The values of the *AP* were normalized. Results

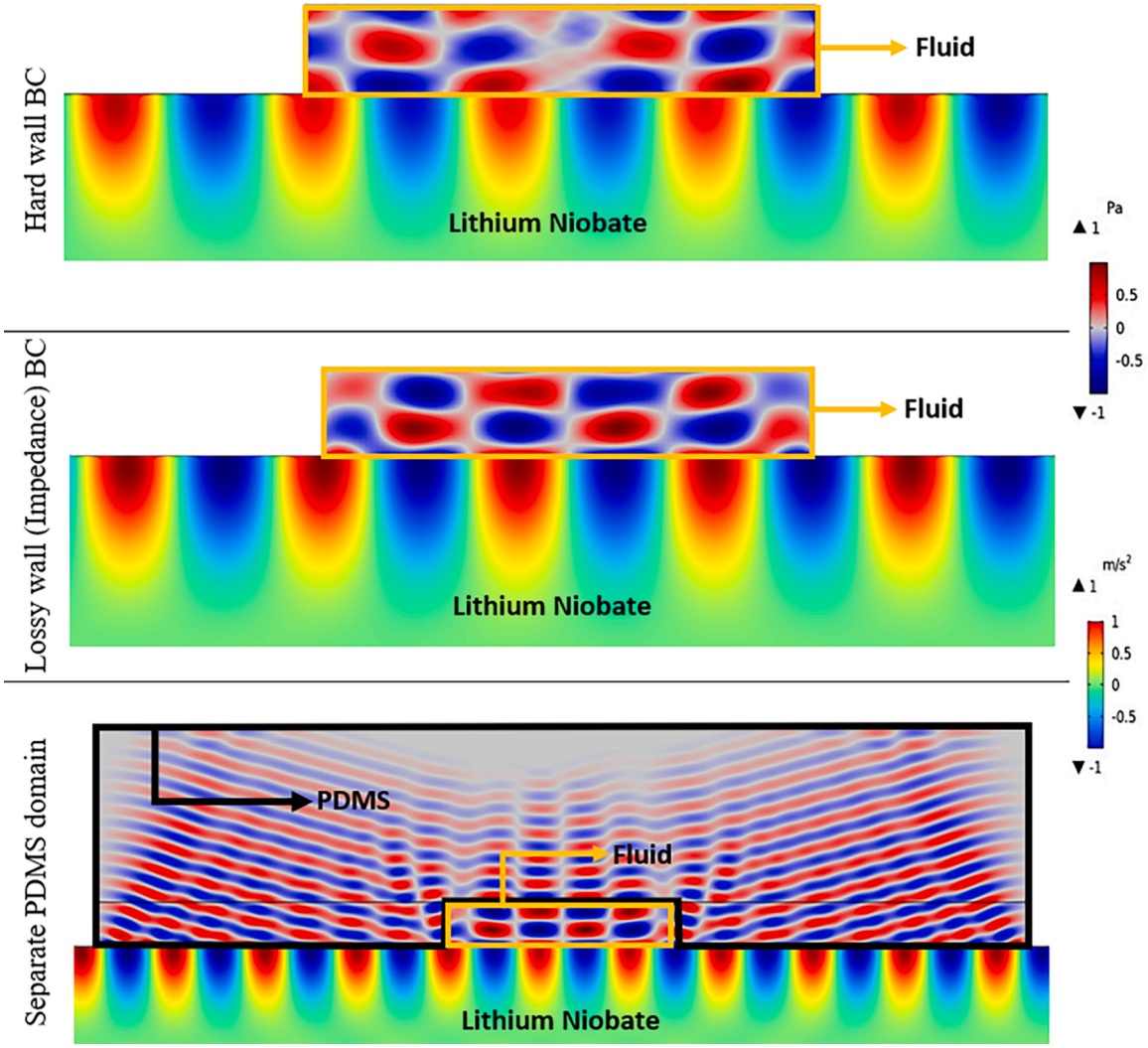


**Fig. 1.** The comparison of the PDMS wall BC effects on the amplitude and the morphology of acoustic pressure distribution and the normal acceleration.

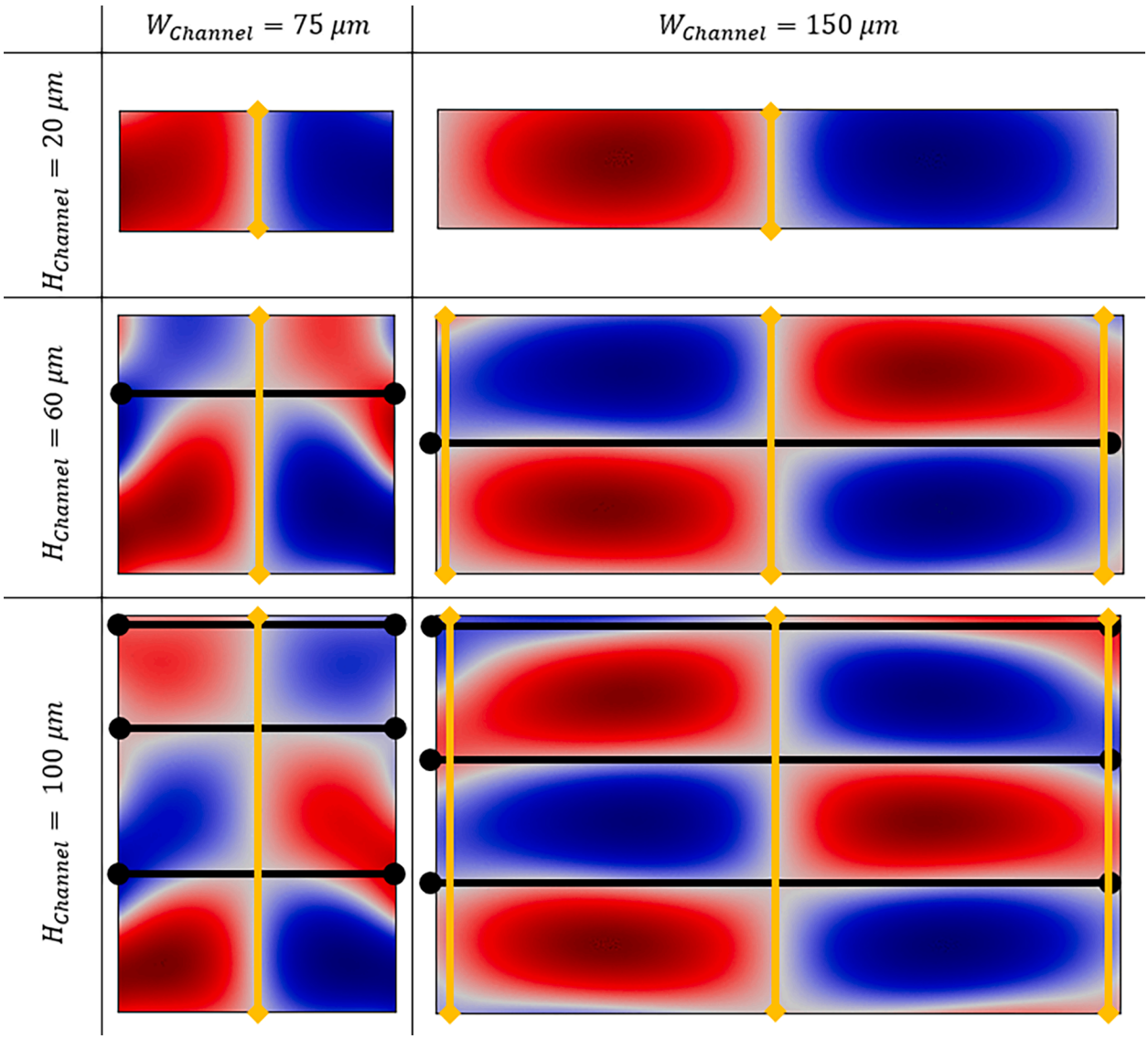


**Fig. 2.** The distribution of pressure nodes (PNs) and pressure anti-nodes (PANs) at different widths and heights of the microchannel. The yellow and black color bars show the location of the vertical and horizontal PN lines, respectively. (For interpretation of the references to color in this figure legend, the reader is referred to the web version of this article.)

indicate that the height of 20$\mu m$ provides only a vertical PN (yellow bars), while greater heights promote one and three horizontal PNs (black bars) at heights of 60$\mu m$ and 100$\mu m$, respectively. Additionally, the increase in the height causes the occurrence of multiple *AP* dipoles (across the height of the microchannel) whose location of them is mirrored concerning the bottom *AP* dipole. While the microchannel's width is half of the wavelength, only one vertical PN occurs in the middle of the microchannel compared to three vertical PNs (i.e., one in the middle and two at sidewalls) when the width of the microchannel is the same as the wavelength. It is worth mentioning that the location of the horizontal PNs changes over time ($T = 1/f_0$); the horizontal PNs and *AP* dipoles move to the top of the microchannel until their energy dissipates to PDMS. As it is shown, there are three PNs when the width = 150$\mu m$. The reason is that the speed of sound in the fluid is different from that in $LiNbO_3$, which causes an inevitable mismatch in the frequency inside the microchannel. Thus, the microchannel was shifted by $\lambda_{SAW}/4$ from the center of the delay line to locate one PN in the middle of the microchannel; otherwise, there would be acoustic pressure disruption due to inaccurate positioning of vertical displacement at the interface of $LiNbO_3$/fluid/PDMS.

### 2.4. Effects of width and height of PDMS

As previously mentioned, sound waves propagate into the PDMS domain before reaching the middle-trapped fluid, dissipating most of its acoustic energy into the PDMS domain. Thus, the effect of the width ($W_{PDMS}$) and height ($H_{PDMS}$) of the PDMS walls on the distribution of the normal component of the displacement ($\delta$) at the surface of $LiNbO_3$ and *AP* inside the microchannel are investigated to minimize energy dissipation. The same parameter values used in the previous section were used for this section except for the width and the height of PDMS.

Fig. 3 shows the correlation between $\delta$ at the interface of $LiNbO_3$/fluid/PDMS for different $W_{PDMS}$ (constant $H_{PDMS}$) and different $H_{PDMS}$ (constant $W_{PDMS}$). Once acoustic waves reach the PDMS domain, they start to propagate in PDMS at the Rayleigh angle, and hence, $\delta$ decreases exponentially before reaching the fluid domain. The results show that the displacement decreases from 30 Å to 15 Å by increasing $W_{PDMS}$ from 1 mm to 4.5 mm at the constant $H_{PDMS}$. However, this behavior was not followed by varying $H_{PDMS}$ (at constant $W_{PDMS}$): not a significant variation in $\delta$ was observed (about a 6% reduction in $\delta$) by increasing $H_{PDMS}$ from 1 mm to 5 mm at the constant $W_{PDMS}$.

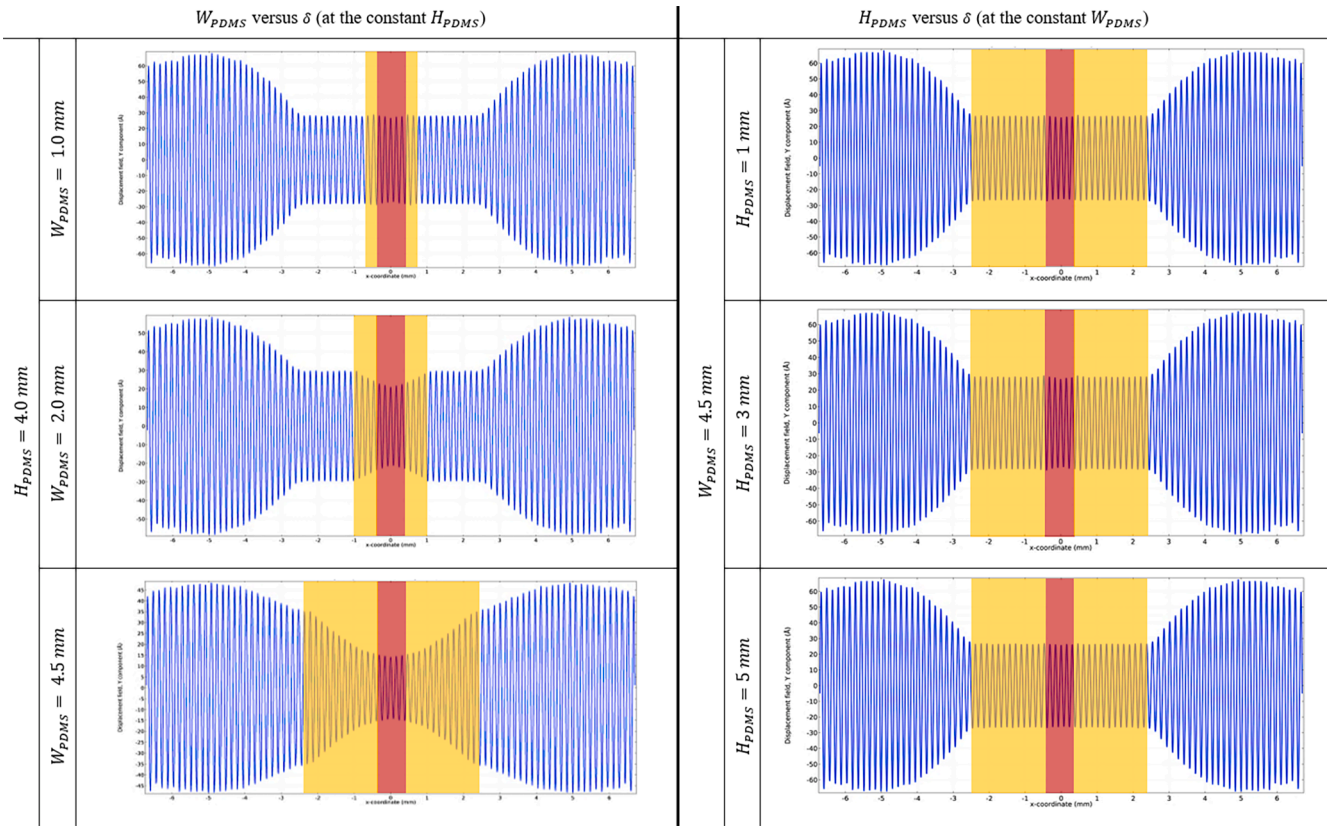


**Fig. 3.** Effects of $W_{PDMS}$ and $H_{PDMS}$ on the normal component of displacement ($\delta$). The red and yellow regions represent fluid and PDMS domains, respectively. (For interpretation of the references to color in this figure legend, the reader is referred to the web version of this article.)

Furthermore, the same trends were followed by the acoustic pressure of the fluid trapped inside the microchannel (see Fig. 4 in which the variation of *AP* inside the microchannel was plotted along the vertical cutline located in the middle of the microchannel). In essence, the acoustic pressure decreases substantially from 1500*kPa* to 900*kPa* by increasing $W_{PDMS}$ from 1 mm to 4.5 mm (at the constant $H_{PDMS} = 5mm$). However, in the vertical cutline (i.e., at a distance of 1.4 mm from the bottom of the PDMS), the *AP* reaches ~0*kPa* indicating that most of the SAW energy is dissipated within 1 mm from the bottom of PDMS. The results indicate that SAW energy dissipation is dependent only on $W_{PDMS}$; $H_{PDMS}$ the modification does not affect the displacement magnitude and the acoustic pressure significantly, and hence will not be considered for the next steps of this study.

It is shown as $H_{PDMS}$ increases, the temperature inside the microchannel and PDMS goes up regardless of the $W_{PDMS}$ value. However, the same behavior is not observed for $W_{PDMS}$ variation at constant $H_{PDMS}$; although bigger $W_{PDMS}$ leads to the lower maximum temperature, these changes are negligible compared to $H_{PDMS}$ variation. Furthermore, the temperature variation along the vertical cutline located inside of PDMS is shown in Fig. S8. It is observed that the temperature delay exponentially as it is distanced from the bottom of the PDMS to its top. Additionally, previous research [42] has shown that the thick *PDMS* can lead

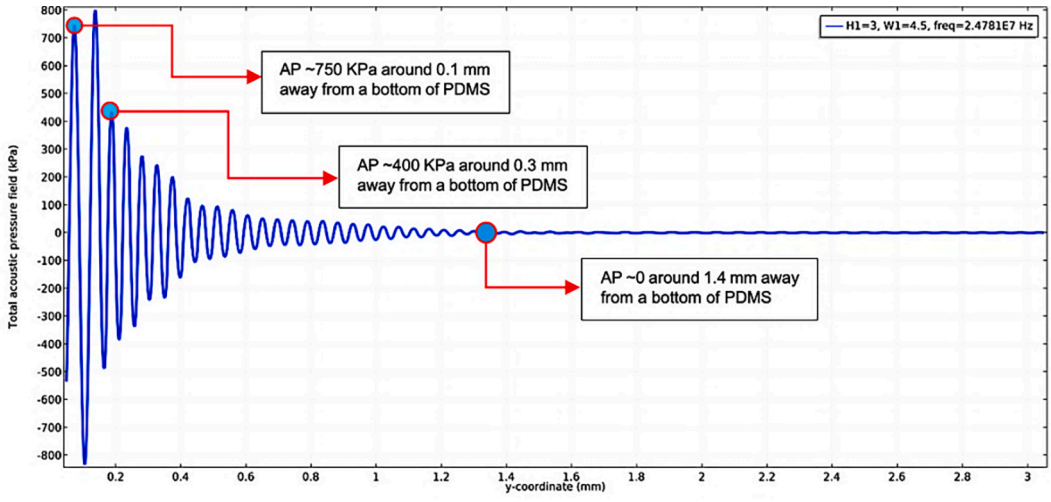


**Fig. 4.** The variation of acoustic pressure (*AP*) at different widths and heights of PDMS along the vertical cutlines.

to the acoustothermal heating of the device in addition to poor acoustic energy transmission. As can be seen from Fig. 5, both and can affect the temperature distribution inside the microchannel and *PDMS*. It is shown as increases, the temperature inside the microchannel and PDMS goes up regardless of the value. However, the same behavior is not observed for variation at constant; although bigger leads to the lower maximum temperature, these changes are negligible compared to variation. Furthermore, the temperature variation along the vertical cutline located inside of PDMS is shown in Fig. S8. It is observed that the temperature delay exponentially as it is distanced from the bottom of the PDMS to its top.

### 2.5. Effects of number of IDT fingers

The number of finger pairs ($N_p$) of IDTs is an important parameter partially due to its effect on the quality factor [43] and the effective piezoelectric coupling coefficient of the substrate. The greater the coupling coefficient, the greater the amount of energy that can be transduced in the IDTs (leading to a higher magnitude of *AP*). The energy transfer goes up by increasing $N_p$ up to the limit of the material [40]. However, the bandwidth reduces due to mismatching that happened in the impedance between IDTs pairs and the signal source [25,40]: when the voltage $V_0$ is applied to IDTs, the power is both absorbed and produced; this behavior is defined by the electrical admittance of the IDTs including capacitance, conductance, and susceptance. At a certain frequency, susceptance becomes negative and begins to counteract with capacitance. When these terms cancel out, the admittance becomes real and directly corresponds to a resistive load and the most efficient operation of the IDTs [17,25]. As the majority of signal generators use a widely accepted standard of 50Ω for their resistive load, a suitable $N_p$ must be used in the final design to match the impedance of the RF signal generator and IDTs [17]. To find a suitable number of IDT fingers providing maximum energy transmission, the relationship between the magnitude of the normal component of displacement (the absolute value) and energy transmission on $N_p$ are studied parametrically. The following parameter values were used for this section: $V_0 = 20V$, $\lambda_{SAW} = 100\mu m$, $W_{Channel} = \lambda_{SAW}/2$, $H_{Channel} = 60\mu m$, $W_{PDMS} = 2mm$, and $H_{PDMS} = 0.5mm$. As can be seen from Fig. 6 (A), $N_P = \{20, 50, 80\}$ provide the maximum magnitude of acceleration which is in good agreement with the previous study [25] (indicating $N_P = 20$ provides the most efficient operation of the IDTs). The same trend was observed for different value of wavelength ($\lambda_{SAW} = \{150, 200\}\mu m$). Interestingly, $N_P$ also affects both magnitude and profile of the mechanical motion at the $LiNbO_3$ and PDMS/fluid interference (See Table S4). $N_P = 20$ has been considered in this study.

In addition, the electromechanical coefficient ($K^2$) was calculated according to Smith's equivalent circuit model by using Eq. (S25). As mentioned previously, since admittance plays an important role in the efficient operation of the IDTs and energy transmission, it was calculated first to derive $K^2$ value for each $N_P$. As it is shown in Fig. 6 (B), the result agrees well with the aforementioned reported data (the normal component of the acceleration versus $N_P$).

### 2.6. Particle trajectories

The "Particle Tracing" module in the COMSOL Multiphysics software package was used to calculate trajectories at various times inside the microchannel. This module evaluates the location of each particle independently at different time frames. Since the cross-section of the acoustofluidic chip was modeled in this study, the drag force imposed by the convection term of the fluid flow was neglected as the direction of the fluid flow ($Z$) is perpendicular to the computational domain and cannot affect $X$ and $Y$ directions of the microparticle motion. For this part of the simulation, 2000 particles were released at time zero second

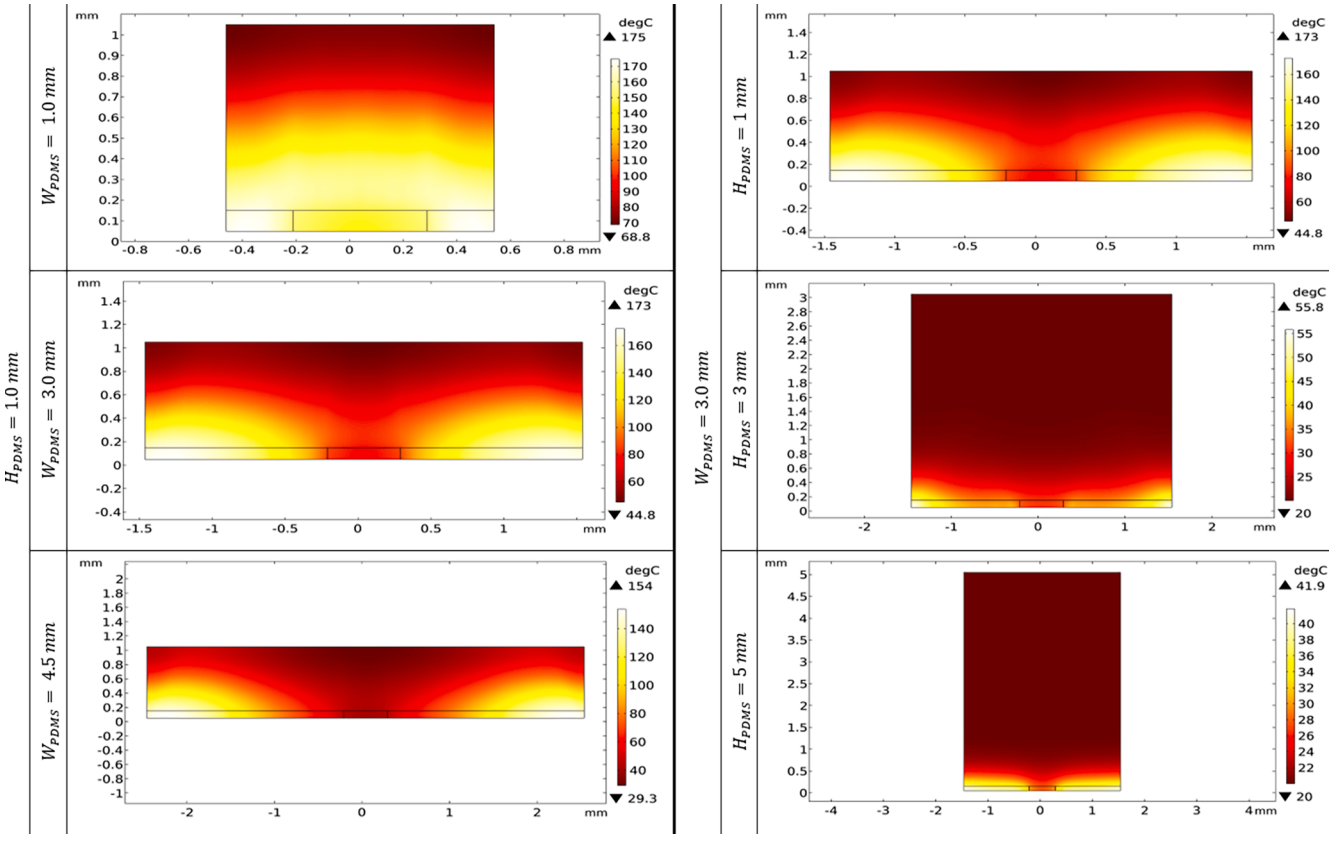


**Fig. 5.** Effects of $W_{PDMS}$ (at the constant $H_{PDMS}$) on the normal component of displacement ($\delta$). The red and yellow regions represent fluid and PDMS domains, respectively. (For interpretation of the references to color in this figure legend, the reader is referred to the web version of this article.)

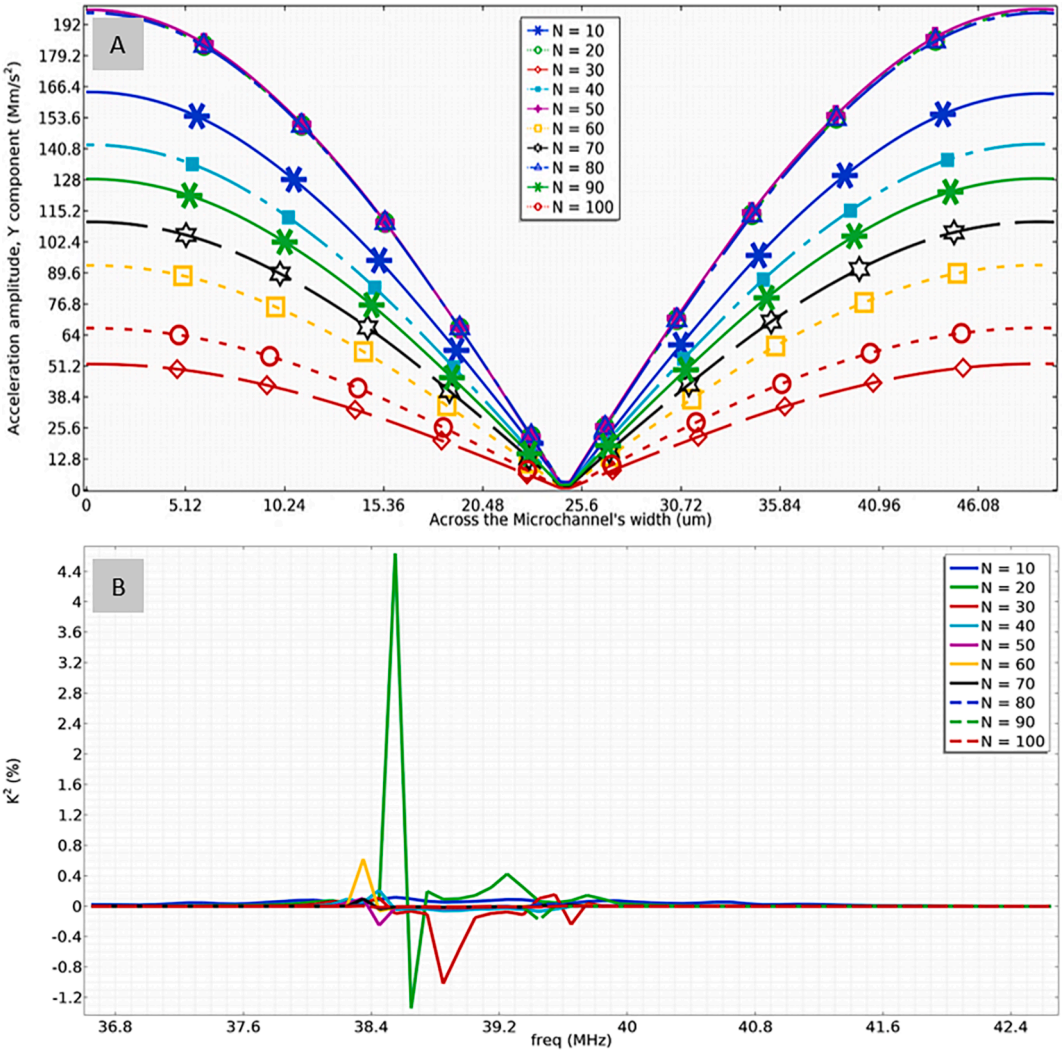


**Fig. 6.** (A) The variation of the normal component of the acceleration across the width of the microchannel for different values of the IDTs fingers, (B) The variation of the electro-mechanical coupling coefficient ($K^2$) for different values of the IDTs fingers around the resonance frequency. The graphs are plotted at.$\lambda_{SAW} = 100\mu m$

and distributed homogenously. Then, the *ARF* and the force induced by the relative velocity of SAW were applied to the particles. The values of the applied parameters were the same as in previous sections; however, to validate the results of this section, the applied *AC* voltage and frequency were adjusted to some extent based on the values of the 1D HSW simulation of Shi et al. [44]. As a result, the following parameter values were used for this section: $V_0 = 5V$, $\lambda_{SAW} = 200\mu m$, $N_p = 20$, $W_{Channel} = \lambda_{SAW}$, $H_{Channel} = 100\mu m$, $W_{PDMS} = 4.5mm$, and $H_{PDMS} = 2.0mm$.

At first, the effects of the frequency and the particle diameter on the particle motion were investigated by the parametric study. Using Eqs. (14) to (17), we evaluated the variation of the horizontal component of the acoustic radiation force ($ARF_x$) along the horizontal cutline passed through the middle of the width of the microchannel width. Note that the microchannel was shifted by $\lambda_{SAW}/4$ to match the location of the PN lines in the fluid. The results are shown in Fig. 7: as the wavelength increases from $100\mu m$ to $200\mu m$, the peak value of $ARF_x$ for the particle with a diameter of $d_P = 10\mu m$ decreases from $110pN$ to $60pN$ (50% reduction). These values matched perfectly with results reported by Shi et al. [44] with a slight deviation in values due to higher input power and a smaller frequency in their study compared to the results presented in this paper.

Additionally, three PNs and two PANs were formed inside the microchannel since the width of the microchannel is equal to the wavelength. The results demonstrate that both PNs and PANs are located where the amplitude of $ARF_x$ reaches zero. Also, PNs only occurs when the direction of $ARF_x$ is inward while the PANs are outward (see Fig. 7). This is due to the fact that the maximum value of $ARF_x$ occurs when the acoustic potential field ($U$) experiences the maximum gradient. The maxima of $U$ are located between each PN and PAN where there is a maximum gradient of $U$. Nonetheless, the gradient of $U$ at PNs and PANs locations is zero due to the occurrence of maxima and minima of the acoustic pressure and acoustic velocity in PANs, respectively as well as zero value of both of them in PNs. Thus, by moving closer to PNs and PANs, the magnitude of $ARF_x$ decreases which cause a longer period for the particle migration toward PNs.

In the next step, the distribution of particles under the influence of *ARF* was simulated. The results are shown in Fig. 8 when the wavelength is $200\mu m$ at various time frames (the calculated optimal values of the previously discussed parameters were used for this step). It can be seen that particles migrate to the middle of the microchannel and along the sidewalls which are the location of the PNs. The required time for the $1\mu m$ particle to move toward the middle PN is significantly longer at a constant wavelength compare to the $5\mu m$particles (as about 99% of the $5\mu m$particles have already reached the middle PN while this value for the $1\mu m$ is about 40%). There is a small difference in the $5\mu m$ particle migration between frames 0.5 s and 1.0 s, which indicates they already have reached their final positions (PN lines) around 0.5 s. These results

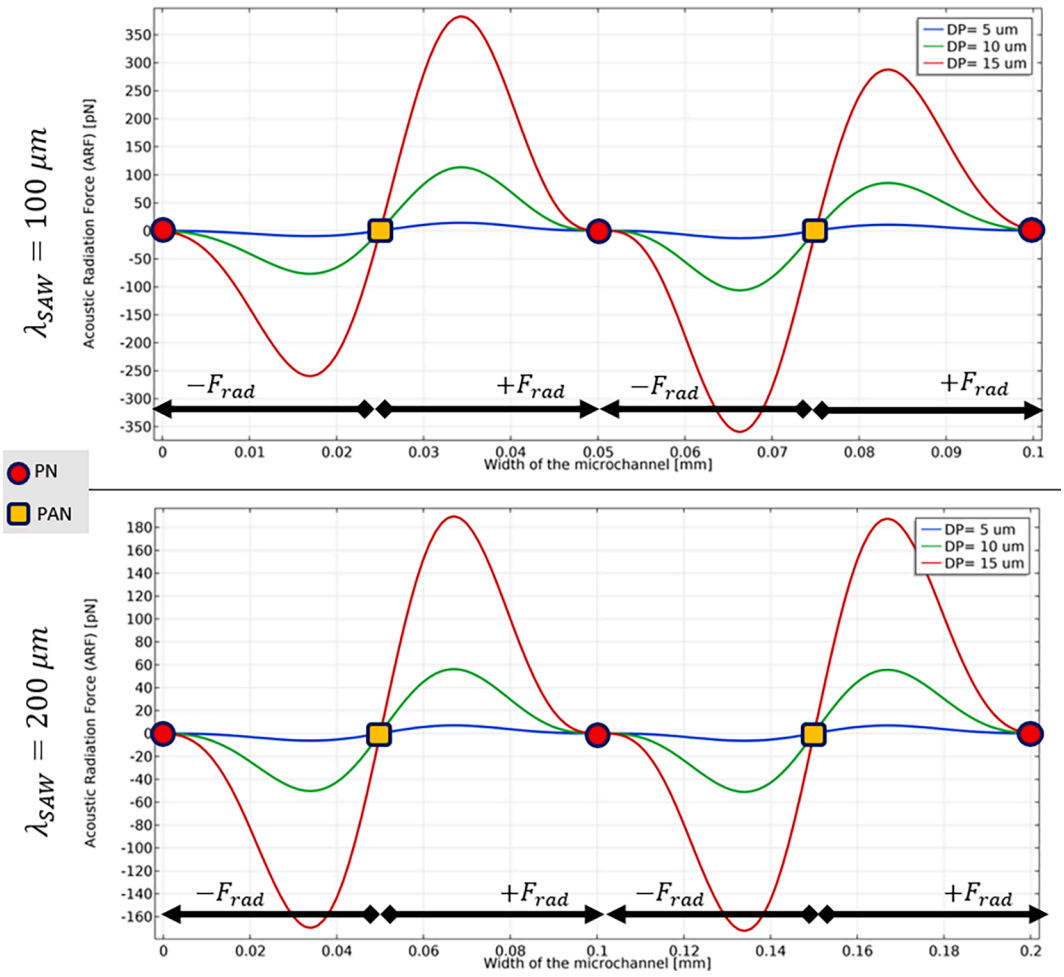


**Fig. 7.** $ARF_x$ distribution across the width of the microchannel at the different wavelengths for particles with a diameter of $d_P = \{5, 10, 15\}\mu m$.

indicate that the time required for particles to complete their migration toward PNs is highly non-linear versus their diameters, which agrees well with the introduced formula by shi et al. [44]. These results qualitatively agree with previous studies: using a 1D HSW numerical simulation, Shi et al. [44] claimed that the required times for $\{5, 1\}\mu m$ particles to move from the sidewalls to the middle PN at $\lambda_{SAW} = 300\mu m$ are ~0.5 s, and ~10 s, respectively. Our results indicated half of these values for the complete migration toward the middle PN (See Video S6). The main reasons for this discrepancy are the higher wavelength (here $\lambda_{SAW} = 200\mu m$ was used while $\lambda_{SAW} = 300\mu m$ similar to Shi et al. [44]). Also, three PN lines were located in the microchannel, and hence the half distance is required for the particles to be positioned entirely at PNs. It is worth mentioning that this mismatch has a higher deviation when smaller particles are considered (around ten times higher in a smaller size ~$1\mu m$ particle compared to ~$5\mu m$ particle). This indicates the importance of migration timing in the successful particle/cell isolation/manipulation purposes. The results in Fig. 8 revealed that *ARF* also has a vertical component acting on the particles and causing their migration in the vertical direction. At the final stages of the particle migration towards PNs, they attached to the sidewalls of the microchannel: if the height of the microchannel is relatively larger than the wavelength, multiples PNs and PANs are created inside the microchannel, causing the particle migration towards not only vertical PNs but also to the horizontal PNs. Considering these two directions of motion, it can be concluded that 1D HSW simulations cannot accurately predict particle migration, and there is always a bias in the results of such simulations.

### 2.7. Effects of dielectrophoresis

As SAW propagates in $LiNbO_3$, the electrical field is generated inside the piezoelectric substrate as well. The main reason behind this phenomenon is piezoelectricity law [25], as the mechanical strain and electrical field are highly coupled with each other. As a result, the fluid in the microchannel is exposed to a direct electrical voltage at the bottom of the microchannel. Thus, lithium niobate acts as an electrode. Herein, we studied the effect of the applied AC voltage amplitude on the amount of the transferred electrical potential to the fluid. The same geometry and operational conditions as before were implemented in this section except for the applied AC voltage amplitude. In essence, the DEP force is proportional to the gradient of the squared of the electric field $\nabla|E|^2$ [18]. Fig. 9 illustrates the variation of $\nabla|E|^2$ components along two cutlines (shown as the yellow bar in Fig. 9): $\left\{\nabla|E|^2\right\}_x$ along the horizontal cutline (which is located at the half of the microchannel's height) and $\left\{\nabla|E|^2\right\}_y$ along the vertical cutline (which is located in the middle of the microchannel's width). As it is shown in Fig. 9, the horizontal component of $\nabla|E|^2$ is proportional to the $V_0$ amplitude where there is a noticeable increase in $\left\{\nabla|E|^2\right\}_x$ value at high voltages ($V_0 = \{20, 25\}V$). Additionally, the value of $\left\{\nabla|E|^2\right\}_x$ becomes zero in the middle of the microchannel where the horizontal PN line is located. Fig. 9 shows the magnitude of $\left\{\nabla|E|^2\right\}_y$ which is higher at the bottom of the microchannel while it is neglectable near the top of the

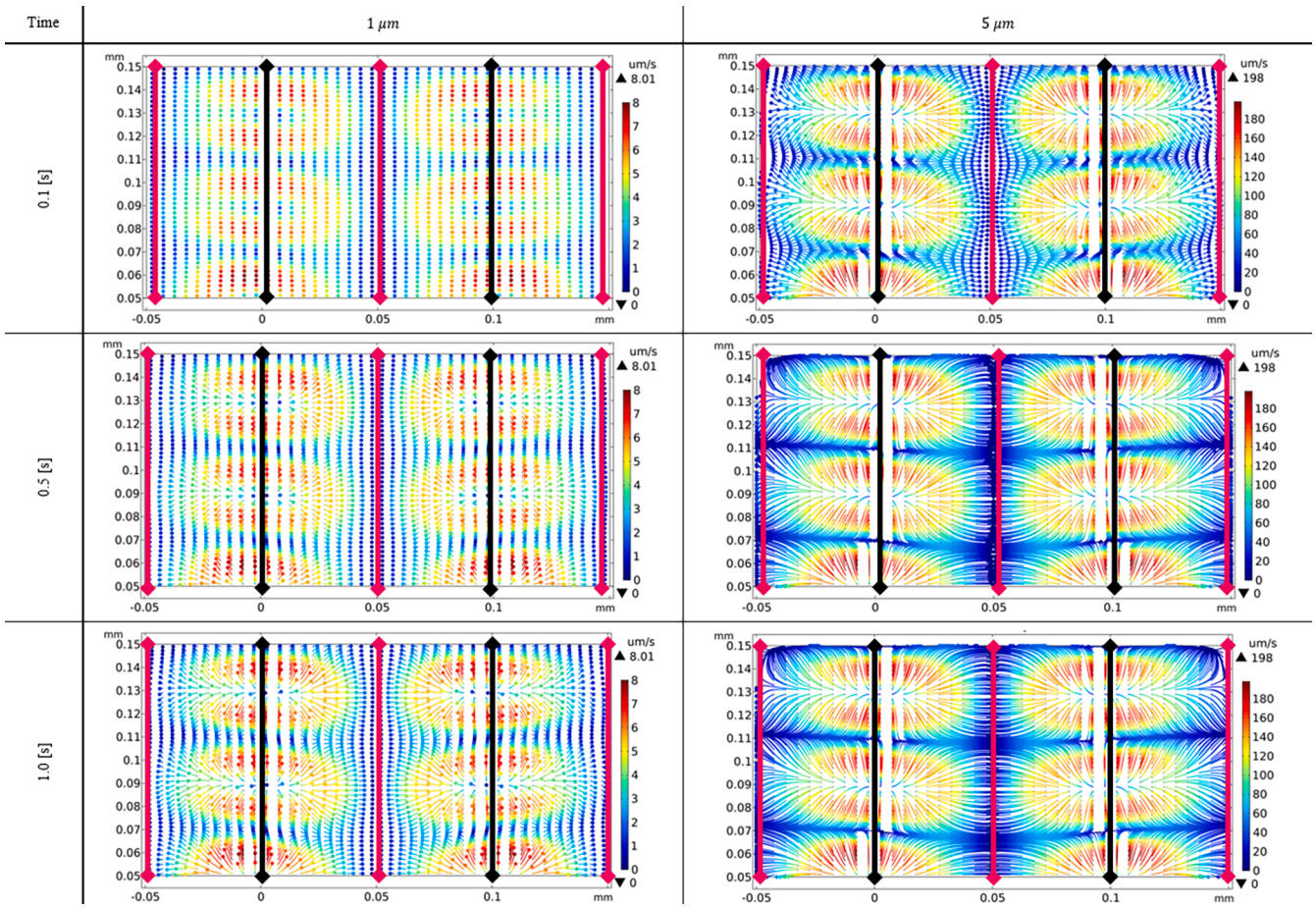


**Fig. 8.** The numerical simulation of the particle distribution under *ARF* influence in two different time frames when $\lambda_{SAW} = 200\mu m$. The particles are shown as points along their pathways they followed from their initial to the final locations. The PNs and PANs locations are shown as the black and dark-pink bars at each time frame. (For interpretation of the references to color in this figure legend, the reader is referred to the web version of this article.)

microchannel. Thus, the vertical component of the electric field pushes the particles toward the upper side of the microchannel. Similar to $\left\{\nabla|E|^2\right\}_x$, there is a direct relationship between $V_0$ and $\left\{\nabla|E|^2\right\}_y$. This result indicates that the DEP force plays an important role at high $V_0$ and must be considered in all of the experiments. The comparison between $\left\{\nabla|E|^2\right\}_x$ and $ARF_x$ indicates that the amplitude of these forces follows the opposite trend (and hence there is a competition between the DEP and *ARF* in the fluid); when $ARF_x$ value is at its smallest value $\left\{\nabla|E|^2\right\}_x$ experiences the local maxima. Although *ARF* is always dominant over the DEP force [45] in SSAW devices, it cannot be neglected completely. Prior to the migration of the particles toward the PN lines, *ARF* dominates the DEP force. However, after migration *ARF* becomes almost zero at the PN lines so DEP force dominates (even though the maximum value of DEP force is smaller compared to the maximum value of *ARF* at the PAN lines). The DEP force leads to the particle aggregation causing exertion of a chaining force ($F_{chain}$) [46,47] due to the interaction of particles when they are close enough to each other. The distribution of the electrical voltage at the top of the $LiNbO_3$ substrate is shown in Fig. S10.

### 2.8. Numerical simulation validation

To validate the results of the presented numerical simulation, they were compared against the simulation results presented by Hsu et al. [48]. The value of the acoustic pressure (*AP*) was considered as the validation parameter. The geometrical parameters and operational conditions were adjusted accordingly: $\lambda_{SAW} = 398\mu m$, $N_p = 8$, $W_{Channel} = 1600\mu m$, $H_{Channel} = 25\mu m$, $W_{PDMS} = 3.2mm$, and $H_{PDMS} = 2.0mm$. Fig. 10 (A) shows the variation of *AP* across the width of the microchannel at the half of the microchannel's height. The results are in great agreement with only a 5% difference.

Next, particle and *AP* distribution were compared against those reported by Hsu et al. [37]. The parameters ($f_{SAW} = 10.02$MHz, $N_p = 20$, $W_{Channel} = 250\mu m$, $H_{Channel} = 25\mu m$, $W_{PDMS} = 1.6mm$, and $H_{PDMS} = 1.0mm$) were adjusted again to match those used in Hsu et al. [37]. Fig. 10 (B) demonstrates the results of this comparison. It is worth mentioning that the value of *AP* was normalized in the graphs, and hence the location of PNs (presented in vertical white dashed lines) are in the dark blue regions. The results of the two studies agree well: the migration paths and the final position (shown as the red dashed line after 1 s) of $8\mu m$ particles coincide well with the previously reported study.

## 3. Experimental results

After validation of the numerical simulation with the previous studies, the optimum parameters suggested by the simulations are used in experimental settings to study further the effect of the particle size, the amplitude of the applied voltage, the number of IDTs, and the dielectrophoresis effect. It is worth mentioning that an acoustic window (*AW*) was not incorporated in the experiments. *AWs* are used to mitigate the loss of acoustic energy to the PDMS before the waves could be coupled with the liquid inside the microchannel [33,49].

The following subsections show the microparticle motion at different

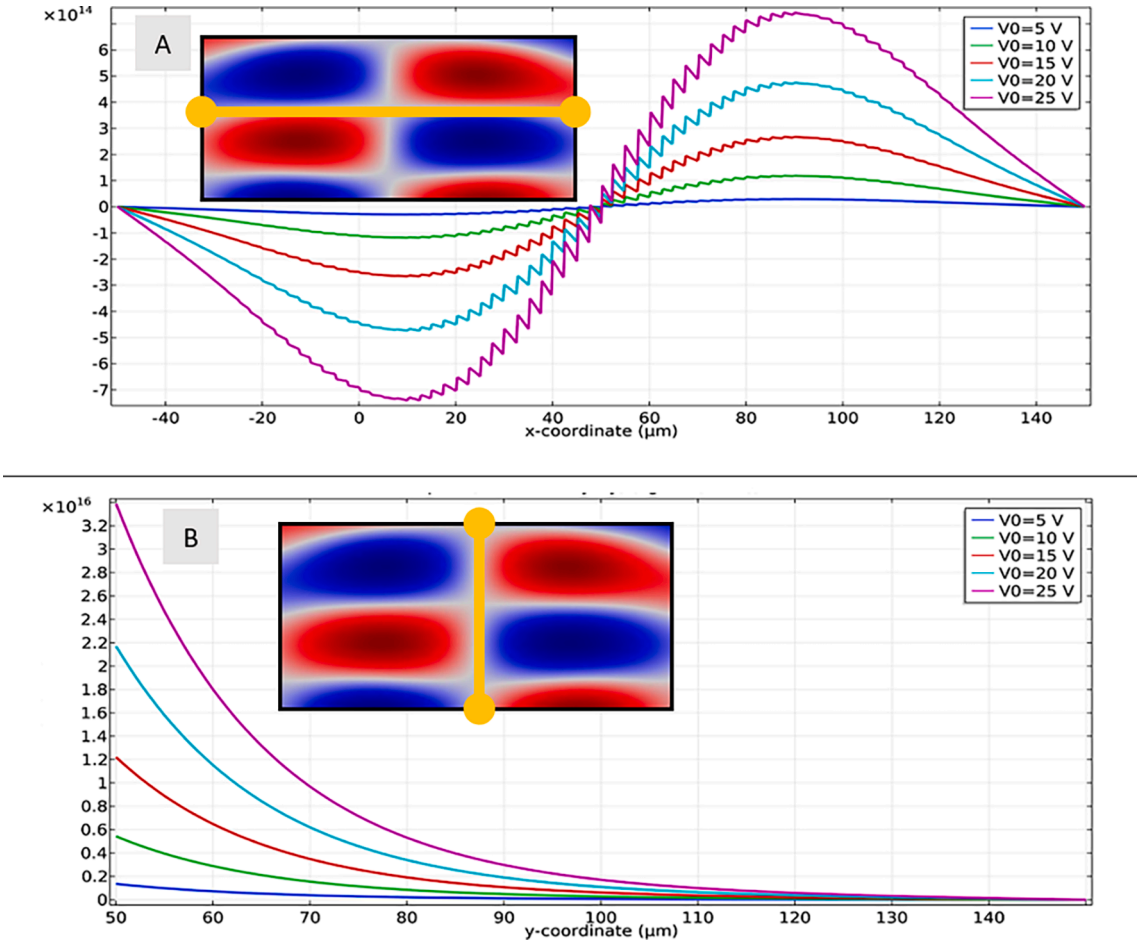


**Fig. 9.** The variation of $\nabla|E|^2$ components along different cutlines located inside the microchannel: (A) the variation of $\left\{\nabla|E|^2\right\}_x$ along the horizontal cutline and (B) The variation of $\left\{\nabla|E|^2\right\}_y$ along the vertical cutline. The yellow bar indicates the location of the cutline. (For interpretation of the references to color in this figure legend, the reader is referred to the web version of this article.)

applied conditions.

### 3.1. Effects of size of particles

*ARF* value has a direct correlation with the AC voltage amplitude applied to IDTs and the volume of the particles. However, if the duration of *ARF* is long enough, all particles, regardless of their size and density, eventually migrate to PNs. Thus, we experimentally studied the time scale for a complete course of the microparticle migration toward PNs. As it is shown in Table 1, the PS particles with the size of 5$\mu m$ (See Video S7) and 10$\mu m$ (See Video S8) were injected with an initial homogenous state. Next, the signal generator applied the RF signal to the IDTs with the amplitude of $V_0 = 10V$ peak-to-peak. The results revealed that 5$\mu m$ and 10$\mu m$ PS particles required time is around 4.0s and 0.5s, respectively, to complete their full migration course toward the nearest PNs. It is worth mentioning that due to the long exposure time of the microscope (for the live recording of particle motion), these time figures are only approximations, which explains the slight difference with the numerical simulation results. These results show a small difference in the time required for 10$\mu m$ PS particles to complete the course of migration toward PNs, which was reported by Guldiken et al. study [2] (here ~0.5 s compared to the reported ~0.1 s). However, this difference increases for 5$\mu m$ PS particles (here ~4.0 s compared to the reported ~1.0 s time). The reason for this deviation can be explained by the influence of other forces which are not negligible for small sizes of particles (such as random motion due to the Brownian force and the particle-to-particle interaction force).

An image analysis tool (MATLAB, version 2019a, Image Processing Toolbox) was also used to quantitatively compare the position of the particles at each PN line along the width of the channel at two-time frames (i.e., the initial and final states). By enhancing the contrast of images, the averaged normalized (by 255) pixel values along each PN line (shown as a red arrow in Table 1) were calculate (see Table 2). Finally, these averaged values are cumulatively averaged for all PN lines (e.g., 0.2393 and 0.4767for 5$\mu m$ PS particles at the initial and final states, respectively; whereas these values are 0.1836 and 0.0468, respectively, for 10$\mu m$ PS particles.). An acoustic radiation coefficient of performance ($COP_{rad}$) was introduced to evaluate the particle migration efficiency.

$$COP_{rad} = \frac{AVE_f}{AVE_i} \tag{21}$$

In the above equation, *f* and *i* subscripts indicate the final and initial states of the particles, respectively.

Using this relation, the values of $COP_{rad}$ 2 and 4 were derived for 5$\mu m$ and 10$\mu m$ PS particles, respectively. This result shows that the $COP_{rad}$ is almost doubled for 10$\mu m$ PS particles compared to that obtained for the5$\mu m$ PS particles which agree well with those estimated from the numerical simulation. Note that there is no direct correlation between $COP_{rad}$ and migration time of particles due to a possible discrepancy in pixel values. Thus, $COP_{rad}$ can be only used as an estimate to evaluate the effectiveness of such devices for each setup configuration.

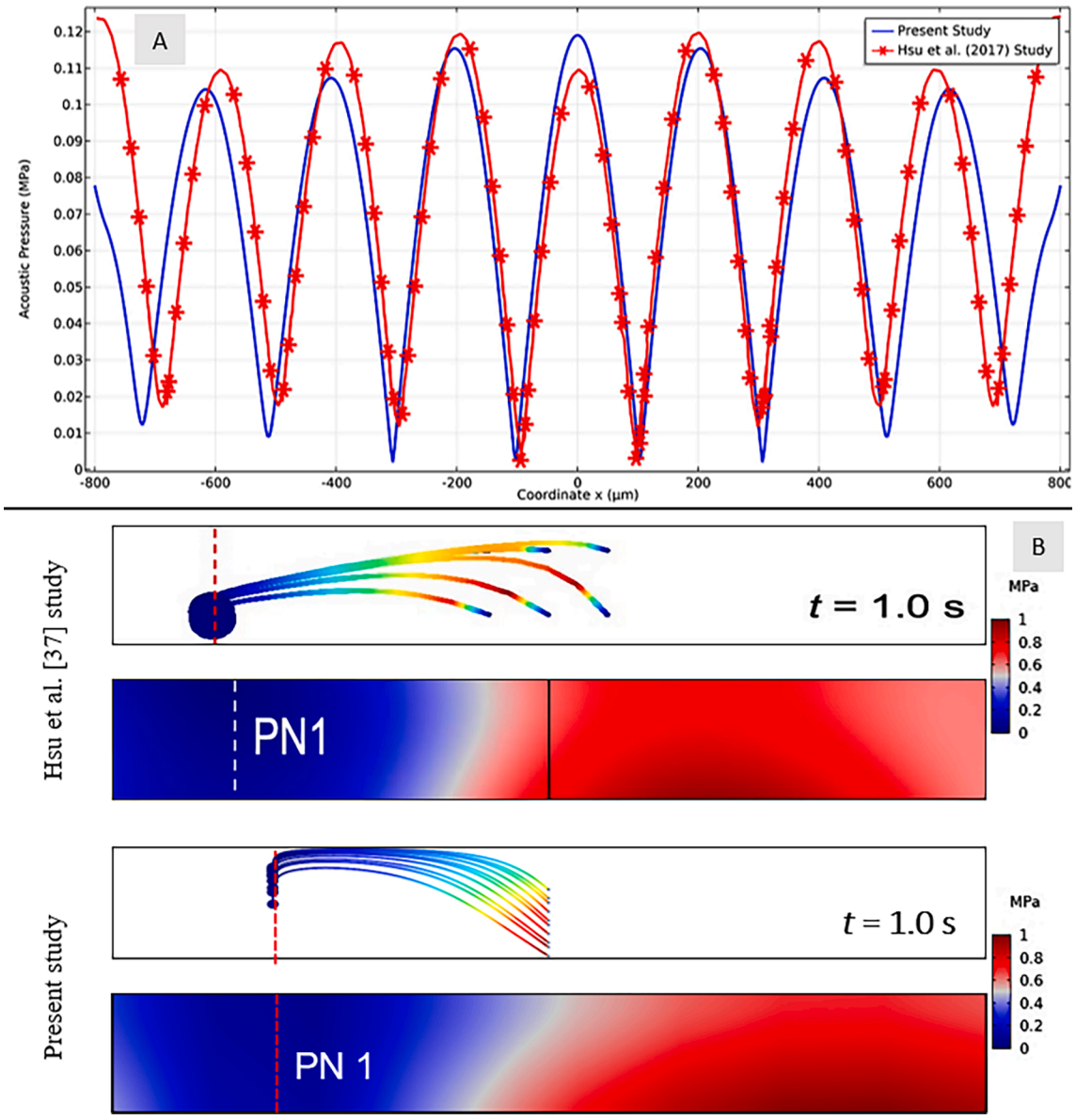


**Fig. 10.** (A) Acoustic pressure (*AP*) distribution across the width of the microchannel (coordinate $x$) at half of the microchannel's height ($12.5\mu m$). The results are from two studies: Hsu et al. [48] (red line) and present study (blue line), (B) The comparison of results of the present study and Hsu et al. work [37] for microparticle migration. (For interpretation of the references to color in this figure legend, the reader is referred to the web version of this article.)

### 3.2. Effects of applied AC voltage amplitude

The amplitude of the applied *AC* voltage has a direct correlation to the magnitude of *AP* and *ARF*: the higher the input power, the higher the efficiency, and the smaller the period required. However, the increase in the input power and hence *ARF* would cause Joule heating, bubble formation, and aggregation of particles inside the microchannel, which can disturb the flow direction, throughput, and functionality of the chip [50]. Herein, we carried out a test to investigate the effect of $V_0$ on $5\mu m$ PS particle migration by increasing $V_0$ with a rate of $1V/s$. For each applied voltage, the corresponding numerical simulation is shown below each corresponding experimental result (see Fig. 11). In essence, as $V_0$ is increased from $0.0V$ to $5.0V$ with an increment of $2.5V$, a large number of PS particles move toward the nearest PNs (almost 30% of the particles have reached PNs by $V_0 = 5.0V$). The same behavior was observed in the numerical simulation results for $V_0 = \{2.5, 5.0\}V$; the majority of $5\mu m$ particles could not complete their migration course completely. Then, we increased $V_0$ from $5.0V$ to $20.0V$ with a rate of $5V/s$ to minimize the impact (bias) of *ARF* action duration. Both numerical and experimental results showed that the majority of the particles reached their nearest PNs by $V_0 = 15.0V$. Nonetheless, we continued increasing the applied voltage in the experiments to investigate the impact of the high voltage on particle movement. The results indicated that at the voltage of $V_0 = 20.0V$ particle aggregation happened which disturbed the flow direction and hence there was no difference in the location of the particles (See Video S9). The numerical results also showed that an increase in the voltage beyond $15.0V$ does not affect the further migration of the particles. The main reason behind this phenomenon is the vertical component of acoustic radiation force ($ARF_y$) which pushes the particles toward the top of the microchannel, and hence due to adhesion between the particles and the microchannel, no motion is observed after that.

### 3.3. Effects of dielectrophoresis

As previously mentioned, the aggregation of particles is an inevitable

**Table 1**
Migration of 5$\mu m$ and 10 $\mu m$ PS particles towards PNs at different time frames. It is worth mentioning that image processing techniques were used to improve the contrast and quality. The following test conditions were used for the test: $\lambda_{SAW} = 200\mu m$, Applied RF signal amplitude = 10[$V$] peak-to-peak, Microchannel's width and height = {800 and 100} [$\mu m$].

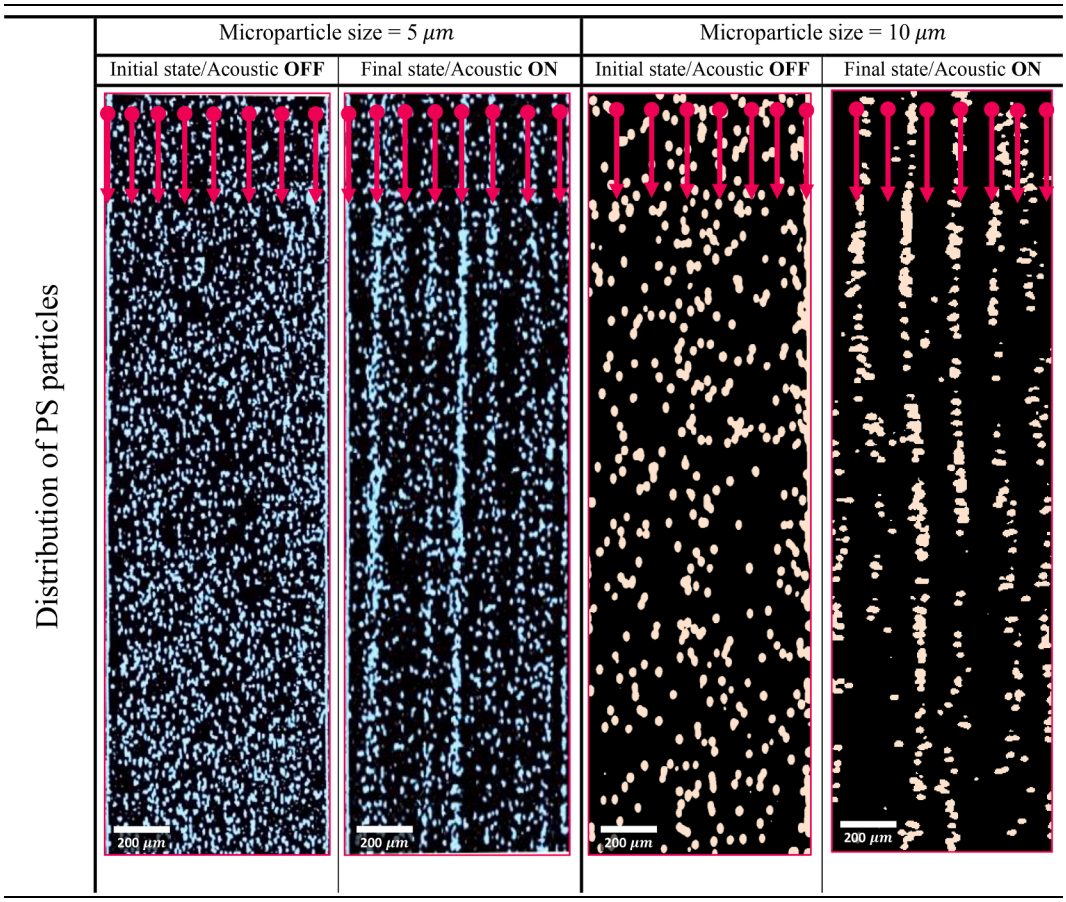


**Table 2**
The Averaged pixel value of the PN lines for 5$\mu m$ and 10$\mu m$ PS particles at the initial and final states.

| PN number | | PN 1 | PN 2 | PN 3 | PN 4 | PN 5 | PN 6 | PN 7 | Average |
|---|---|---|---|---|---|---|---|---|---|
| 5$\mu m$ Microparticle | Final state Acoustic **ON** | 0.4997 | 0.3476 | 0.2695 | 0.4499 | 0.7287 | 0.4344 | 0.6068 | 0.4767 |
| | Initial state Acoustic **OFF** | 0.2363 | 0.2667 | 0.2594 | 0.2315 | 0.2076 | 0.2686 | 0.2048 | 0.2393 |
| 10$\mu m$Microparticle | Final state Acoustic **ON** | 0.1746 | 0.1684 | 0.1815 | 0.2082 | 0.1909 | 0.1929 | 0.1685 | 0.1836 |
| | Initial state Acoustic **OFF** | 0.0695 | 0.0391 | 0.0522 | 0.0709 | 0.0378 | 0.0304 | 0.0277 | 0.0468 |

phenomenon in high *AC* voltages in acoustofluidic devices. Herein, the effect of high applied voltages was investigated. The value of parameters are as follows: $\lambda_{SAW} = 100\ \mu m$, $N_P = 20$, Microparticle size = 5$\mu m$, microchannel's width = 800$\mu m$, microchannel's height = 100 $\mu m$. As can be seen from Fig. 12, more aggregation occurs over time when constant high *AC* electrical voltage ($V_0 = 25V$) is applied. Interestingly, the aggregation followed not only PN line locations (here the microchannel was tilted a little bit due to the misalignment in the bonding process) but also formed separate clusters at each PN line (See Video S10), which was previously claimed in [5,47,51]. The results are also in agreement with those provided by the FEA simulation in the previous section. Thus, and the effect of *DEP* cannot be neglected in the acoustofluidic device.

## 4. Conclusion

One of the goals of this study was to demonstrate the capability of the acoustofluidic chip as a highly precise and fast-acting platform for manipulation and separation of particles. Various steps were taken into account to achieve this goal, including carrying out the parameter optimization, developing the 2D numerical simulation, and conducting experiments. As a first step, the proposed lab-on-a-chip acoustofluidic chip was studied parametrically by the FEM method. The numerical simulation derived the optimum values of the parameters. Next, these optimized parameters were implemented to validate the outcomes of the numerical simulation with the experimental tests. The simulation results indicated that the applied voltage and the number of IDT fingers play an essential role in the efficiency of the acoustofluidic chip. As expected, there is a direct correlation between *ARF* and the applied voltage. Furthermore, the need for precise alignment has been shown: a small

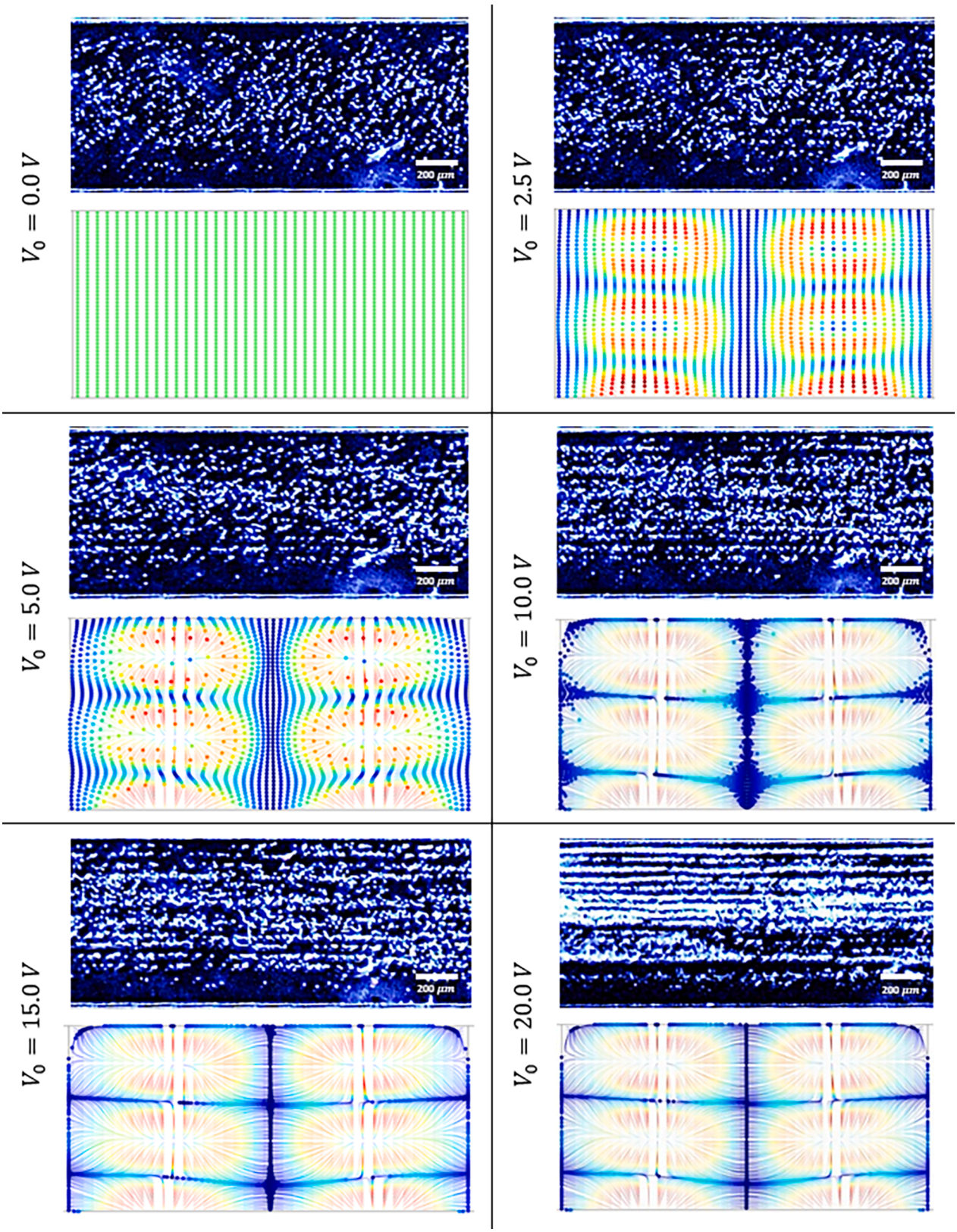


**Fig. 11.** Displacement of 5$\mu m$ PS particles at the various applied RF signals amplitude when $\lambda_{SAW} = 200\mu m$.

shift in the microchannel location can disturb the morphology of *ARF* in the fluid completely.

In order to validate the outcome of the numerical simulation, the experimental setup was prepared based on the derived optimum values from the numerical simulation results. Both experimental and numerical results indicated the importance of various geometrical parameters and operational conditions such as applied AC voltage and number of fingers of IDTs: $V_0 = 15.0V$ is the maximum value of the applied voltage supplied to the chip to ensure stable tests. Additionally, it was shown numerically that only $N_p = \{20, 50, 80\}$ provide the highest energy

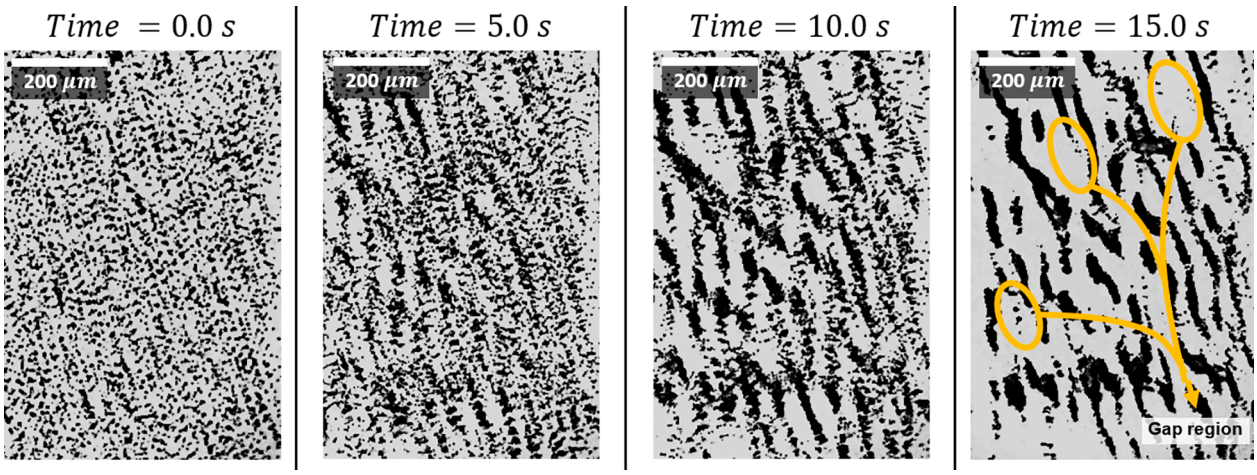


**Fig. 12.** The particle migration at high applied RF values at different time frames. The gap regions are formed.

transfer and a small variation from the optimum $N_p$ would cause a substantial reduction in *ARF*. Another interesting outcome of the FEA simulation is the effect of PDMS thickness. The results demonstrated that the acoustic energy dissipation could be prevented if the width of PDMS is smaller than 1 mm. Furthermore, the presence of dielectrophoresis must be considered at high applied AC voltages. The presented results in this work provide a guideline for the future design of acoustofluidic chips with higher reproducibility and efficiency. However, there are a few aspects in the presented study recommended for future studies: e.g., a similar study must be repeated with the bioparticles as there is a slight variation in some of their physical properties (such as compressibility) compared to PS particles. Additionally, the 3D numerical simulation should be conducted to cover both parametric study and particle tracing together.

## CRediT authorship contribution statement

**Erfan Taatizadeh:** Conceptualization, Methodology, Software, Validation, Investigation, Resources, Writing - original draft, Writing - review & editing, Visualization. **Arash Dalili:** Investigation. **Pamela Inés Rellstab-Sánchez:** Investigation. **Hamed Tahmooressi:** Writing - original draft. **Adithya Ravishankara:** Visualization. **Nishat Tasnim:** Writing - original draft. **Homayoun Najjaran:** Resources. **Isaac T.S. Li:** Supervision, Funding acquisition, Writing - original draft, Writing - review & editing. **Mina Hoorfar:** Supervision, Funding acquisition, Project administration, Writing - original draft, Writing - review & editing.

## Declaration of Competing Interest

The authors declare that they have no known competing financial interests or personal relationships that could have appeared to influence the work reported in this paper.

## Appendix A. Supplementary data

Supplementary data to this article can be found online at https://doi.org/10.1016/j.ultsonch.2021.105651.

## References

[1] S. Li, F. Ma, H. Bachman, C.E. Cameron, X. Zeng, T.J. Huang, Acoustofluidic bacteria separation, J. Micromech. Microeng. 27 (1) (2016), 015031.
[2] R. Guldiken, M.C. Jo, N.D. Gallant, U. Demirci, J. Zhe, Sheathless size-based acoustic particle separation, Sensors 12 (1) (2012) 905–922.
[3] X. Li, et al., Challenges and opportunities in exosome research—perspectives from biology, engineering, and cancer therapy, APL Bioeng. 3 (1) (2019), 011503.
[4] T. Salafi, K.K. Zeming, Y. Zhang, Advancements in microfluidics for nanoparticle separation, Lab. Chip 17 (1) (2017) 11–33.
[5] A. Dalili, E. Samiei, M. Hoorfar, A review of sorting, separation and isolation of cells and microbeads for biomedical applications: microfluidic approaches, Analyst 144 (1) (2019) 87–113.
[6] R.T. Davies, J. Kim, S.C. Jang, E.-J. Choi, Y.S. Gho, J. Park, Microfluidic filtration system to isolate extracellular vesicles from blood, Lab. Chip 12 (24) (2012) 5202–5210.
[7] H.-K. Woo, et al., Exodisc for rapid, size-selective, and efficient isolation and analysis of nanoscale extracellular vesicles from biological samples, ACS Nano 11 (2) (2017) 1360–1370.
[8] L.-G. Liang, et al., An integrated double-filtration microfluidic device for isolation, enrichment and quantification of urinary extracellular vesicles for detection of bladder cancer, Sci. Rep. 7 (2017) 46224.
[9] M. He, J. Crow, M. Roth, Y. Zeng, A.K. Godwin, Integrated immunoisolation and protein analysis of circulating exosomes using microfluidic technology, Lab. Chip 14 (19) (2014) 3773–3780.
[10] S.S. Kanwar, C.J. Dunlay, D.M. Simeone, S. Nagrath, Microfluidic device (ExoChip) for on-chip isolation, quantification and characterization of circulating exosomes, Lab. Chip 14 (11) (2014) 1891–1900.
[11] J.S. Dudani, D.R. Gossett, H.T. Tse, R.J. Lamm, R.P. Kulkarni, D.D. Carlo, Rapid inertial solution exchange for enrichment and flow cytometric detection of microvesicles, Biomicrofluidics 9 (1) (2015), 014112.
[12] Z. Zhao, Y. Yang, Y. Zeng, M. He, A microfluidic ExoSearch chip for multiplexed exosome detection towards blood-based ovarian cancer diagnosis, Lab. Chip 16 (3) (2016) 489–496.
[13] J.C. Yeo, Z. Kenry, P. Zhao, Z.W. Zhang, C.T. Lim, Label-free extraction of extracellular vesicles using centrifugal microfluidics, Biomicrofluidics 12 (2) (2018), 024103.
[14] B.H. Wunsch, et al., Nanoscale lateral displacement arrays for the separation of exosomes and colloids down to 20 nm, Nat. Nanotechnol. 11 (11) (2016) 936.
[15] C. Liu, et al., Field-free isolation of exosomes from extracellular vesicles by microfluidic viscoelastic flows, ACS Nano 11 (7) (2017) 6968–6976.
[16] M. Wu, et al., Isolation of exosomes from whole blood by integrating acoustics and microfluidics, Proc. Natl. Acad. Sci. (2017) 201709210.
[17] K. Lee, H. Shao, R. Weissleder, H. Lee, Acoustic purification of extracellular microvesicles, ACS Nano 9 (3) (2015) 2321–2327.
[18] A. Dalili, E. Taatizadeh, M. Hoorfar, Characterization of the electrodes of DEP-based micro-separator, 2018.
[19] A. Urbansky, P. Ohlsson, A. Lenshof, F. Garofalo, S. Scheding, T. Laurell, Rapid and effective enrichment of mononuclear cells from blood using acoustophoresis, Sci. Rep. 7 (1) (2017) 17161.
[20] A. Arnau, Piezoelectric Transducers and Applications, vol. 2004, Springer, 2004.
[21] I. Leibacher, P. Reichert, J. Dual, Microfluidic droplet handling by bulk acoustic wave (BAW) acoustophoresis, Lab. Chip 15 (13) (2015) 2896–2905, https://doi.org/10.1039/C5LC00083A.
[22] K. Länge, B.E. Rapp, M. Rapp, Surface acoustic wave biosensors: a review, Anal. Bioanal. Chem. 391 (5) (2008) 1509–1519.
[23] M.-I. Rocha-Gaso, C. March-Iborra, Á. Montoya-Baides, A. Arnau-Vives, Surface generated acoustic wave biosensors for the detection of pathogens: a review, Sensors 9 (7) (2009) 5740–5769.
[24] J.C. Andle, J.F. Vetelino, M.W. Lade, D.J. McAllister, An acoustic plate mode biosensor, Sens. Actuators B Chem. 8 (2) (1992) 191–198.
[25] W. Connacher et al., Micro/nano acoustofluidics: materials, phenomena, design, devices, and applications, Lab. Chip, 2018.
[26] X. Ding, et al., Surface acoustic wave microfluidics, Lab. Chip 13 (18) (2013) 3626–3649.
[27] M. Gedge, M. Hill, Theory of surface acoustic wave devices for particle manipulation, in: Microscale Acoustofluidics, Royal Society of Chemistry, 2014, pp. 337–353.
[28] G. Destgeer, H.J. Sung, Recent advances in microfluidic actuation and micro-object manipulation via surface acoustic waves, Lab. Chip 15 (13) (2015) 2722–2738.

[29] A.M. Soliman, M.A. Eldosoky, T.E. Taha, The separation of blood components using standing surface acoustic waves (SSAWs) microfluidic devices: analysis and simulation, Bioengineering 4 (2) (2017) 28.
[30] G. Destgeer, A. Alazzam, H.J. Sung, High frequency travelling surface acoustic waves for microparticle separation, J. Mech. Sci. Technol. 30 (9) (2016) 3945–3952.
[31] A. Renaudin, J.-P. Sozanski, B. Verbeke, V. Zhang, P. Tabourier, C. Druon, Monitoring SAW-actuated microdroplets in view of biological applications, Sens. Actuators B Chem. 138 (1) (2009) 374–382.
[32] G. Destgeer, B.H. Ha, J.H. Jung, H.J. Sung, Submicron separation of microspheres via travelling surface acoustic waves, Lab. Chip 14 (24) (2014) 4665–4672.
[33] X. Ding, et al., Cell separation using tilted-angle standing surface acoustic waves, Proc. Natl. Acad. Sci. 111 (36) (2014) 12992–12997.
[34] Z. Mao, Y. Xie, F. Guo, L. Ren, P.-H. Huang, Y. Chen, J. Rufo, F. Costanzo, T. J. Huang, Experimental and numerical studies on standing surface acoustic wave microfluidics, Lab. Chip 16 (3) (2016) 515–524.
[35] L. Johansson, J. Enlund, S. Johansson, I. Katardjiev, V. Yantchev, Surface acoustic wave induced particle manipulation in a PDMS channel—principle concepts for continuous flow applications, Biomed. Microdevices 14 (2) (2012) 279–289.
[36] N. Nama, R. Barnkob, Z. Mao, C.J. Kähler, F. Costanzo, T.J. Huang, Numerical study of acoustophoretic motion of particles in a PDMS microchannel driven by surface acoustic waves, Lab. Chip 15 (12) (2015) 2700–2709.
[37] J.-C. Hsu, C.-H. Hsu, Y.-W. Huang, Acoustophoretic control of microparticle transport using dual-wavelength surface acoustic wave devices, Micromachines 10 (1) (2019) 52.
[38] P.B. Muller, R. Barnkob, M.J.H. Jensen, H. Bruus, A numerical study of microparticle acoustophoresis driven by acoustic radiation forces and streaming-induced drag forces, Lab. Chip 12 (22) (2012) 4617–4627.
[39] J. Lee, C. Rhyou, B. Kang, H. Lee, Continuously phase-modulated standing surface acoustic waves for separation of particles and cells in microfluidic channels containing multiple pressure nodes, J. Phys. Appl. Phys. 50 (16) (2017), 165401.
[40] M.C. Jo, An Acoustic-based Microfluidic Platform for Active Separation and Mixing, 2013.
[41] J. Guo, Y. Kang, Y.e. Ai, Radiation dominated acoustophoresis driven by surface acoustic waves, J. Colloid Interface Sci. 455 (2015) 203–211.
[42] B.H. Ha, K.S. Lee, G. Destgeer, J. Park, J.S. Choung, J.H. Jung, J.H. Shin, H.J. Sung, Acoustothermal heating of polydimethylsiloxane microfluidic system, Sci. Rep. 5 (1) (2015), https://doi.org/10.1038/srep11851.
[43] D. Morgan, Surface Acoustic Wave Filters: With Applications to Electronic Communications and Signal Processing, Academic Press, 2010.
[44] J. Shi, H. Huang, Z. Stratton, Y. Huang, T.J. Huang, Continuous particle separation in a microfluidic channel via standing surface acoustic waves (SSAW), Lab. Chip 9 (23) (2009) 3354–3359.
[45] P. Sehgal, B.J. Kirby, Separation of 300 and 100 nm particles in fabry-perot acoustofluidic resonators, Anal. Chem. 89 (22) (2017) 12192–12200, https://doi.org/10.1021/acs.analchem.7b02858.
[46] O.D. Velev, K.H. Bhatt, On-chip micromanipulation and assembly of colloidal particles by electric fields, Soft Matter 2 (9) (2006) 738–750.
[47] T. Zheng, C. Wang, C. Xu, Q. Hu, S. Wei, Patterning microparticles into a two-dimensional pattern using one column standing surface acoustic waves, Sens. Actuators Phys. 284 (2018) 168–171.
[48] J.-C. Hsu, Y.-W. Huang, C.-H. Hsu, Transportation control of microfluidic particles using mode switching between surface acoustic waves and plate waves, Jpn. J. Appl. Phys. 56 (7S1) (2017) 07JD05.
[49] J. Park, G. Destgeer, H. Kim, Y. Cho, H.J. Sung, In-droplet microparticle washing and enrichment using surface acoustic wave-driven acoustic radiation force, Lab. Chip 18 (19) (2018) 2936–2945.
[50] R. Zhang, Acoustic Isolation of Extracellular Vesicles, 2016.
[51] A. Dalili, E. Taatizadeh, H. Tahmooressi, N. Tasnim, P.I. Rellstab-Sánchez, M. Shaunessy, H. Najjaran, M. Hoorfar, Parametric study on the geometrical parameters of a lab-on-a-chip platform with tilted planar electrodes for continuous dielectrophoretic manipulation of microparticles, Sci. Rep. 10 (1) (2020), https://doi.org/10.1038/s41598-020-68699-4.